

Plug-and-Play ADMM Based Radar Range Profile Reconstruction Using Deep Priors

Kudret Akçapınar^{1,*}, Naime Özben Önhon², Özgür Gürbüz¹, and Müjdat Çetin³

¹Faculty of Engineering and Natural Sciences, Sabancı University, Tuzla, İstanbul 34956, Türkiye

²Faculty of Engineering, Turkish-German University, Turkey

³Department of Electrical and Computer Engineering, University of Rochester, Rochester, NY 14627, USA

ABSTRACT: Reconstructing a range profile from radar returns, which are both noisy and band-limited, presents a challenging and ill-posed inverse problem. Conventional reconstruction methods often involve employing matched filters in pulsed radars or performing a Fourier transform of the received signal in continuous wave radars. However, both of these approaches rely on specific models and model-based inversion techniques that may not fully leverage prior knowledge of the range profiles being reconstructed when such information is accessible. To incorporate prior distribution information of the range profile data into the reconstruction process, regularizers can be employed to encourage specific spatial patterns within the range profiles. Nevertheless, these regularizers often fall short in effectively capturing the intricate spatial correlations within the range profile data, or they may not readily allow for analytical minimization of the cost function. Recently, Alternating Direction Method of Multipliers (ADMM) framework has emerged as a means to provide a way of decoupling the model inversion from the regularization of the priors, enabling the incorporation of any desired regularizer into the inversion process in a plug-and-play (PnP) fashion. In this paper, we implement an ADMM framework to address the radar range profile reconstruction problem where we propose to employ a Convolutional Neural Network (CNN) as a regularization method for enhancing the quality of the inversion process which usually suffers from the ill-posed nature of the problem. We demonstrate the efficacy of deep learning networks as a regularization method within the ADMM framework through our simulation results. We assess the performance of the ADMM framework employing CNN as a regularizer and conduct a comparative analysis against alternative methods under different measurement scenarios. Notably, among the methods under investigation, ADMM with CNN as a regularizer stands out as the most successful method for radar range profile reconstruction.

1. INTRODUCTION

Range profile formation plays a pivotal role in various radar applications, including runway radar surveillance [1] and the automatic target recognition of high-resolution radar systems [2], where achieving high-quality range resolution is of great significance. This process involves the estimation of reflectivity for each radar range cell and constitutes an inherently challenging inverse problem. The primary goal is to reconstruct the range profile of a scene using radar return measurements at a specific viewing angle. These radar returns are characterized by bandwidth limitations and are often affected by measurement noise, primarily attributed to receiver electronics.

Traditional range profile formation typically hinges on the mathematical inversion of the measurement model. This is typically accomplished by applying Fourier Transform (FT) to the measurements in Frequency Modulated Continuous Wave (FMCW) radar as in [3] or passing measurements through a matched-filtering/pulse-compression blocks in the context of pulsed radar as in [4] to compress the return signals. Nonetheless, the efficacy of these approaches is significantly constrained by the available bandwidth, and they do not consider any prior knowledge about the range profile. To introduce prior knowledge into the inversion process, one can embrace regular-

ized inversion. This involves minimizing a cost function, typically composed of a data-fidelity term and a regularization term. The data fidelity term ensures that the reconstructed range profile aligns with the measurements, while the regularization term accentuates specific features in the reconstructed range profile.

Through regularization, it becomes possible to mitigate the challenges introduced by the ill-posed nature of the inverse problems. For instance, a regularized deconvolution technique is used in [5] to improve the range resolution of a ground-penetrating radar. Point-based and region-based features are enhanced through regularization in synthetic aperture radar (SAR) imaging, as demonstrated by in [6]. Likewise, sparsity-based regularization has found application in near-field multiple-input multiple-output (MIMO) radar imaging [7]. Nevertheless, in any regularized inversion scheme, regularizers often fall short of capturing intricate and hidden data features, as they inherently tend to emphasize fixed and predefined characteristics based on prior assumptions about the reconstructed field, whether in its original space or a transformed one.

As a proximal method, the ADMM framework [8] has garnered substantial attention in the realm of computational imaging as it is possible to separate the optimization of data fidelity and priors within this framework. ADMM has found diverse

* Corresponding author: Kudret Akçapınar (kudret@sabanciuniv.edu).

applications, ranging from computational tomographic imaging [9] to Synthetic Aperture Radar (SAR) imaging applications [10].

The ADMM framework allows for the optimization of the data fidelity and prior terms to be treated as independent modules with their updates occurring in alternating steps during the ADMM iterations. Consequently, the modularity of the ADMM framework enables the use of any regularizer in a plug-and-play fashion, as in [11, 12]. This “plug-and-play” approach empowers the incorporation of various denoisers as a way of regularization within the ADMM framework, all while leaving the data fidelity optimization steps untouched. Various types of denoisers have been applied across a spectrum of applications, including B3MD [13], Total Variation (TV) [14], Recursive Filter (RF) [15], and Non-Local Means (NLM) [16].

PnP ADMM framework has been applied to the field of radar imaging, yielding superior image reconstruction performance. [17] introduces a PnP ADMM framework for SAR image reconstruction, integrating convolutional neural networks (CNNs) as regularizers. Similarly, [18] and [19] employ this approach for sparse ISAR imaging. In [18], the PnP ADMM framework is extended to the so-called PAN architecture, where all parameters in the reconstruction, denoising, and multiplier update layers are learned through end-to-end training via back-propagation. In [17], separate CNNs are trained for diverse measurement conditions. However, in practice, the measurement conditions such as the signal-to-noise ratio (SNR) of radar echo signals from targets is often uncertain. Hence, a practical solution capable of performing consistently across a wide range of SNR values is necessary. Considering this issue and drawing inspiration from [17], in this work, we present a PnP ADMM framework for radar range profile reconstruction for frequency-modulated continuous wave (FMCW) radar, in which the variable SNR conditions arising in practical scenarios are addressed. We demonstrate the potential of using a CNN trained on a dataset with mixed SNR levels, proposing a method that utilizes a single network for this purpose. This approach therefore enhances efficiency and practical applicability, ensuring robust performance across varying SNR conditions.

We begin by establishing an observation/measurement model for a side-looking FMCW radar. After obtaining a discrete observation model that relates the radar measurements to the unknown range profiles we seek to estimate, we formulate the problem within the ADMM framework, effectively isolating the model inversion step from the prior optimization step. To capture and learn the intricate spatial patterns within the radar range profile, we introduce a denoising CNN as a regularizer and train it using our proprietary dataset, derived from Gotcha SAR data. Through our simulations, we rigorously evaluate the performance of the ADMM-based range profile reconstruction method and compared it against various alternative approaches including conventional methods.

We believe that the proposed technique holds promise for enhancing the performance of range profile reconstruction in side-looking radar systems. In summary, our contributions to the radar literature encompass the following: We provide a comprehensive formulation of the range profile reconstruction

problem for side-looking radar systems, presenting both continuous and discrete observation models. We derive the sub-optimization problems within the ADMM framework along with their respective solutions, offering a systematic approach to solving the reconstruction problem. We provide an iterative algorithm to execute the ADMM steps efficiently, facilitating the implementation of our approach in practical radar systems. We implement a denoising convolutional neural network (CNN) to capture complex spatial patterns in range profile data. Our method is capable of performing across varying SNR conditions as it utilizes a single network trained on mixed SNR data.

The remainder of this paper is structured as follows. In Section 2, we present the derivation of both continuous and discrete observation models for a side-looking FMCW radar. Section 3 delves into the inverse problem of radar range profile reconstruction, elucidating the ADMM steps from a Bayesian perspective. Additionally, we provide an in-depth explanation of how we tackle the ADMM subproblems within this section. Our simulation results are detailed and discussed in Section 4. Finally, we conclude with a summary of our findings in Section 5.

2. OBSERVATION MODEL FOR SIDE-LOOKING MONO-STATIC RADAR

We focus on the range profile formation problem in side-looking mono-static imaging radars in this paper. A highly simplified representation of this imaging setup is described in Figure 1(a), where a side-looking radar is illuminating a radar scene shown with the grey footprint to measure the range profile information associated with its look angle. Range profile is the reflectivity of the radar scene along the look angle direction and a representative range profile is shown in Figure 1(a) with Δr denoting a radar range cell. Since each scatterer in a given range cell is assumed to be equidistant to the radar, they contribute to the reflectivity of that range cell. Therefore, the range profile can be considered as the projection of the equidistant scatters onto a specific distance r . Each range profile captures a slice from the reflectivity map of the radar scene. For a mono-static setup, the radar beam is typically steered to different directions either mechanically or electronically to scan the entire radar scene. At each scan angle, the radar returns are stored in a matrix. Through specific procedures applied to this matrix, we generate an image that represents the illuminated scene. A radar typically transmits chirp signals of the following form:

$$s(t) = \cos\left(\omega_0 t + \frac{1}{2} m t^2\right), \quad 0 \leq t \leq T_c \quad (1)$$

with a linearly increasing instantaneous frequency in time with a slope of m such that $\omega(t) = \omega_0 + m t$. The instantaneous frequency $\omega(t)$ of the chirp increases for T_c seconds, then returns to its initial value, ω_0 after sweeping a band of $\Delta\omega = m T_c$. This continuous cycle of transmission is shown in Figure 1(b). The echo signal from a point target located at a radial distance of R_0 will arrive at the radar after two-way propagation delay of $\tau_0 = \frac{2R_0}{c}$, where c is the speed of light in free-space. Therefore,

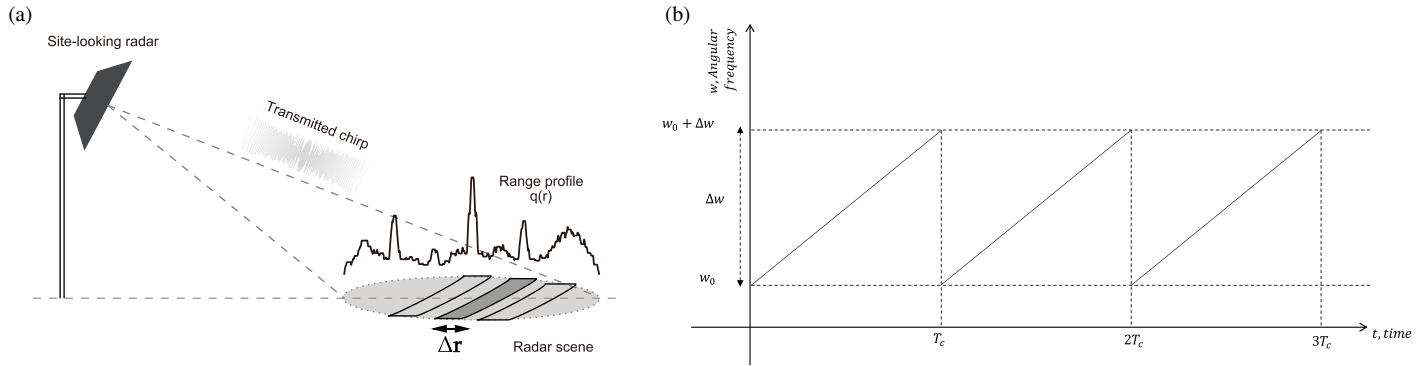


FIGURE 1. Measurement setup & FMCW waveform. (a) Simplified representation of a side-looking radar observation scenario. (b) FMCW waveform.

the received echo signal from a point target is the amplitude-scaled and time-shifted version of the transmitted signal $s(t)$ as follows:

$$a(t) = A_0 \cos \left(\omega_0(t - \tau_0) + \frac{1}{2} m(t - \tau)^2 + \theta_0 \right) \quad (2)$$

Here, $A_0 = |A_0|e^{j\theta_0}$ is the complex-valued reflectivity of the point scatterer. Let $f(x, y)$ denote the reflectivity map of the 2D scene illuminated by the radar. If we take equidistant point scatterers on a slice from this scene as shown in Figure 1(a), then $q(r)$ would be the sum of the reflectivity contribution from each of these scatterers as a function of radial distance, r , and can be expressed as the Radon transform of the reflectivity function $f(x, y)$ [20].

$$q(r) = \iint_{\{x, y\} \in S} f(x, y) \delta(u - x \cos \theta - y \sin \theta) dx dy \quad (3)$$

This is the projection of the reflectivity field onto a single point at a distance of r . Here S represents the total scene illuminated by the radar. The received signal at the receiver is then given by the convolution of the projection of the reflectivity function and the transmitted signal:

$$b(t) = \int_{R_{\min}}^{R_{\max}} q(r) s \left(t - \frac{2r}{c} \right) dr \quad (4)$$

where R_{\min} and R_{\max} denote two ends of the radar scene in the radial direction. By plugging (1) into (4) we obtain

$$b(t) = \int_{R_{\min}}^{R_{\max}} q(r) \cos \left(\omega_0 \left(t - \frac{2r}{c} \right) + \frac{1}{2} m \left(t - \frac{2r}{c} \right)^2 \right) dr \quad (5)$$

The received signal given in (5) is the integral sum of signals from each scatterer in the scene, which are time-shifted and amplitude-scaled. The received signal is then mixed with $2 \cos(\omega_0 t + \frac{1}{2} m t^2)$ and $2 \sin(\omega_0 t + \frac{1}{2} m t^2)$ and passed through a low-pass filter to obtain in-phase $I(t)$ and quadrature

$Q(t)$ components of the received signal. Letting $\bar{r}(t)$ denote the complex demodulated equivalent of the received signal in (5), we can write it as follows:

$$\bar{r}(t) = I(t) + jQ(t) \quad (6)$$

So, using Euler's identity, $\bar{r}(t)$ is represented in the following equivalent complex baseband representation

$$\bar{r}(t) = \int_{R_{\min}}^{R_{\max}} q(r) \exp \left\{ -j \left[m \left(\frac{2r}{c} \right) t + \omega_0 \left(\frac{2r}{c} \right) \right] \right\} dr$$

where we have ignored the term $\frac{1}{2} m \left(\frac{2r}{c} \right)^2$ since $4mr^2 \ll c^2$. Letting $\Omega(t) = \frac{2}{c}(\omega_0 + mt)$, $\bar{r}(t)$ boils down to the following nice form

$$\bar{r}(t) = \int_{R_{\min}}^{R_{\max}} q(r) \exp \{-j\Omega(t)r\} dr \quad (7)$$

Note that (7) is the band-limited spatial Fourier transform of the projections, $q(r)$. Here $\Omega(t)$ represents the spatial frequency variable. Since both the observation time (i.e., chirp time, T_C) and chirp slope are finite, $\Omega(t)$ is limited to a finite band. It is also worthwhile to note that $\Omega(t)$ is offset with an amount of ω_0 from the origin of the Fourier space. One important parameter that can be derived from (7) is the radar range resolution, which determines the minimum distance between two scatterers required to be resolved as two different peaks in the range profile data. Considering a single point scatterer in the range profile, if we take its Fourier transform and bandlimit the spectrum to a finite band, B , and take the inverse Fourier transform to go back to the spatial domain, what we get back is a one-dimensional sinc function. As bandwidth B gets larger, the sinc function becomes more squeezed, giving rise to a sharper peak in the range profile data. This is also called Point Spread Function (PSF), and it fully characterizes any linear space-invariant imaging system by revealing the impulse response of the system. The Rayleigh resolution criterion is the difference between the first null positions of the PSF and is determined by the available bandwidth. Rayleigh range resolution of a radar is given by $\delta r = \frac{c}{2B}$.

The relation between the radar measurements and the range profile given in (7) can be discretized once the range profile $q(r)$ is uniformly sampled with a sampling interval of Δr into N range bins such that

$$q(r) = \sum_{k=0}^{N-1} q[k] \delta(r - k\Delta r) \quad (8)$$

where $q[k]$ denotes the sampled value of the range profile at the i th range cell. Substituting (8) into (7), we obtain

$$\bar{r}(t) = \int_{R_{\min}}^{R_{\max}} \left(\sum_{k=0}^{N-1} q[k] \delta(r - k\Delta r) \right) \exp\{-j\Omega(t)r\} dr \quad (9)$$

which is further simplified to

$$\bar{r}(t) = \sum_{k=k_0}^{k_0+N-1} q[k] \exp\{-j\Omega'(t)k\} \quad (10)$$

with $\Omega'(t) = \Omega(t)\Delta r$. After the discretization of the received signal $\bar{r}(t)$, the discrete observation model with the additive measurement noise can be formulated as follows:

$$\mathbf{r} = \mathbf{T}\mathbf{q} + \mathbf{w} \quad (11)$$

where $\mathbf{T} \in \mathbb{C}^{(M \times N)}$ is a known matrix which describes the measurement model, with M denoting the number of radar measurements and N denoting the number of radar range cells to be estimated. In the case of our scenario, measurement matrix \mathbf{T} is specifically the spatial Discrete Fourier Transform (DFT) operator and $\mathbf{w} \in \mathbb{C}^{(N \times 1)}$ is measurement noise. $\mathbf{r} \in \mathbb{C}^{(M \times 1)}$ is radar measurements and $\mathbf{q} \in \mathbb{C}^{(N \times 1)}$ is the range profile which we want to estimate from the measurements. Estimating radar range profiles from noisy radar measurements is an inverse problem. This inverse problem may not have an exact solution due to the measurement noise presence or may have infinitely many solutions if the null-space of measurement matrix is not empty. For ill-conditioned measurement matrices, the measurement noise can be amplified during inversion. To make the solution more robust against the noise and possible perturbations in the measurement data, as a common approach, inverse problems are usually regularized by leveraging prior knowledge about the underlying unknown vector. In the next section, we will formulate a regularized problem from a Bayesian perspective and construct the ADMM steps.

3. PLUG-AND-PLAY RANGE PROFILE FORMATION

We start our problem formulation by assigning Bayesian probabilities to the parameters in Equation (11). Let $p_{\mathbf{q}}(\mathbf{q})$ and $p_{\mathbf{r}}(\mathbf{r})$ be the probability density functions (pdf) of priors and measurements, respectively. Let $p_{\mathbf{r}|\mathbf{q}}(\mathbf{r}|\mathbf{q})$ denote the conditional probability density, which fully characterizes how \mathbf{r} stores information about \mathbf{q} , generally specified by the measurement model, which in our case involves the linear operator \mathbf{T} and the measurement noise \mathbf{w} . Let us also use $\hat{\mathbf{q}}(\mathbf{r})$ to denote our estimate of \mathbf{q} based on the observation vector \mathbf{r} . In the Bayesian approach,

we choose the “best” estimator based on a performance metric. For this purpose, we define a cost function $C(\mathbf{x}, \hat{\mathbf{x}})$, which returns the cost of estimating an arbitrary vector \mathbf{x} by $\hat{\mathbf{x}}$. Then the “optimal” estimator is the one which minimizes this expected cost. When the following cost function is chosen,

$$C(\mathbf{q}, \hat{\mathbf{q}}) = \begin{cases} 1, & \text{if } |\mathbf{q} - \hat{\mathbf{q}}| > \epsilon \\ 0, & \text{otherwise} \end{cases} \quad (12)$$

in the limiting case where ϵ approaches to zero ($\lim_{\epsilon \rightarrow 0}$), we obtain “Maximum A Posteriori”, shortly MAP estimator. That is,

$$\begin{aligned} \hat{\mathbf{q}}_{\text{MAP}} &= \arg \max_{\mathbf{q}} \{ \log(p_{\mathbf{q}|\mathbf{r}}(\mathbf{q}|\mathbf{r})) \} \\ &= \arg \max_{\mathbf{q}} \{ \log(p_{\mathbf{r}|\mathbf{q}}(\mathbf{r}|\mathbf{q})) + \log(p_{\mathbf{q}}(\mathbf{q})) \} \end{aligned} \quad (13)$$

Assuming that measurement noise samples are independent and identically distributed from a complex Gaussian distribution with a variance of σ^2 , pdf of \mathbf{w} is given by:

$$p_{\mathbf{w}}(\mathbf{w}) \propto \exp\left(-\frac{1}{2\sigma^2} \|\mathbf{w}\|_2^2\right)$$

In this case, the likelihood has the following pdf:

$$p_{\mathbf{r}|\mathbf{q}}(\mathbf{r}|\mathbf{q}) \propto \exp\left(-\frac{1}{2\sigma^2} \|\mathbf{r} - \mathbf{T}\mathbf{q}\|_2^2\right) \quad (14)$$

Let us define the following pdf for the priors:

$$p_{\mathbf{q}}(\mathbf{q}) \propto \exp(-\mu\mathcal{R}(\mathbf{q})) \quad (15)$$

and substitute (14) and (15) into (13), where maximization becomes minimization after a sign-change:

$$\hat{\mathbf{q}}_{\text{MAP}} = \arg \min_{\mathbf{q}} \left\{ \frac{1}{2\sigma^2} \|\mathbf{r} - \mathbf{T}\mathbf{q}\|_2^2 + \mu\mathcal{R}(\mathbf{q}) \right\}$$

Defining the data fidelity as $\mathcal{D}(\mathbf{q}) = \|\mathbf{r} - \mathbf{T}\mathbf{q}\|_2^2$ and letting $\lambda = 2\sigma^2\mu$, MAP estimator in (16) can be written as:

$$\hat{\mathbf{q}}_{\text{MAP}} = \arg \min_{\mathbf{q}} \{ \mathcal{D}(\mathbf{q}) + \lambda\mathcal{R}(\mathbf{q}) \} \quad (16)$$

This is a weighted sum of data fidelity and prior terms. While λ can in principle be determined through the noise and prior pdf parameters, in practice neither of those is perfectly known, hence one needs to tune λ or use a data-driven automated selection method. $\lambda \in \mathbb{R}^+$ serves as a control parameter which determines the relative strength of the data fidelity and prior terms.

3.1. Formation of ADMM Sub-Problems

In order to be able to formulate problem (16) in the ADMM framework, we start by splitting variable \mathbf{q} as follows:

$$(\hat{\mathbf{q}}, \hat{\mathbf{h}}) = \arg \min_{\mathbf{q}, \mathbf{h}} \{ \mathcal{D}(\mathbf{q}) + \lambda\mathcal{R}(\mathbf{h}) \} \quad \text{s.t. } \mathbf{q} - \mathbf{h} = 0 \quad (17)$$

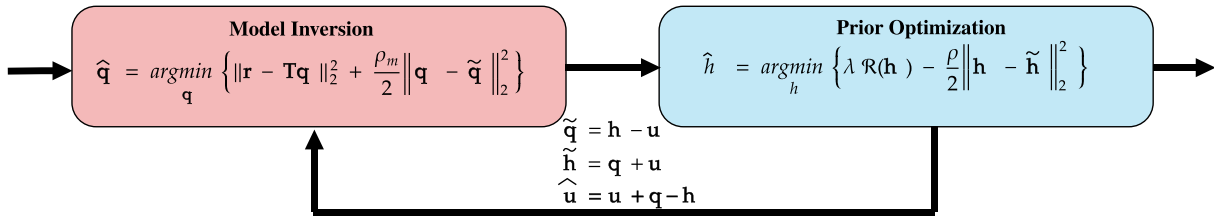


FIGURE 2. A block diagram representation of alternating optimization steps of ADMM.

The augmented Lagrangian for (17) is given by

$$\mathcal{L}(\mathbf{q}, \mathbf{h}, \mathbf{y}) = \mathcal{D}(\mathbf{q}) + \lambda \mathcal{R}(\mathbf{h}) + \mathbf{y}^T (\mathbf{q} - \mathbf{h}) + \frac{\rho}{2} \|\mathbf{q} - \mathbf{h}\|_2^2 \quad (18)$$

where \mathbf{y} is the Lagrange multiplier, and $\rho > 0$ is the penalty parameter. Having defined the augmented Lagrangian objective function, we set the ADMM iterations as follows:

$$\mathbf{q}_{k+1} := \underset{\mathbf{q} \in \mathbb{C}^{(N \times 1)}}{\operatorname{argmin}} \mathcal{L}(\mathbf{q}_k, \mathbf{h}_k, \mathbf{y}_k) \quad (19a)$$

$$\mathbf{h}_{k+1} := \underset{\mathbf{h} \in \mathbb{C}^{(N \times 1)}}{\operatorname{argmin}} \mathcal{L}(\mathbf{q}_{k+1}, \mathbf{h}_k, \mathbf{y}_k) \quad (19b)$$

$$\mathbf{y}_{k+1} := \mathbf{y}_k + \rho(\mathbf{h}_{k+1} - \mathbf{q}_{k+1}) \quad (19c)$$

with k denoting the ADMM iteration number. As a more common version, ADMM can be written in a scaled form. For this purpose, we define a residual vector, $\mathbf{v} = \mathbf{q} - \mathbf{h}$. Then last two terms in the augmented Lagrangian in (18) is

$$\begin{aligned} \mathbf{y}^T \mathbf{v} + \frac{\rho}{2} \|\mathbf{v}\|_2^2 &= \mathbf{y}^T \mathbf{v} + \frac{\rho}{2} \|\mathbf{v}\|_2^2 + \frac{1}{2\rho} \|\mathbf{y}\|_2^2 - \frac{1}{2\rho} \|\mathbf{y}\|_2^2 \\ &= \left\| \sqrt{\frac{\rho}{2}} \mathbf{v} + \frac{1}{\sqrt{2\rho}} \mathbf{y} \right\|_2^2 - \frac{1}{2\rho} \|\mathbf{y}\|_2^2 \\ &= \frac{\rho}{2} \|(\mathbf{v} + \mathbf{u})\|_2^2 - \frac{\rho}{2} \|\mathbf{u}\|_2^2 \end{aligned} \quad (20)$$

where we have added and subtracted $\frac{1}{2\rho} \|\mathbf{y}\|_2^2$ and defined $\mathbf{u} = \frac{1}{\rho} \mathbf{y}$ as a scaled dual variable. With this substitution, the augmented Lagrangian objective function in scaled form is given by

$$\mathcal{L} = \mathcal{D}(\mathbf{q}) + \lambda \mathcal{R}(\mathbf{h}) + \frac{\rho}{2} \|(\mathbf{q} - \mathbf{h} + \mathbf{u})\|_2^2 - \frac{\rho}{2} \|\mathbf{u}\|_2^2$$

The local minima of \mathcal{L} can be found by solving the following sub-minimization problems:

$$\mathbf{q}_{k+1} := \underset{\mathbf{q} \in \mathbb{C}^{(N \times 1)}}{\operatorname{argmin}} \mathcal{L}(\mathbf{q}, \mathbf{h}_k, \mathbf{u}_k) \quad (21a)$$

$$\mathbf{h}_{k+1} := \underset{\mathbf{h} \in \mathbb{C}^{(N \times 1)}}{\operatorname{argmin}} \mathcal{L}(\mathbf{q}_{k+1}, \mathbf{h}, \mathbf{u}_k) \quad (21b)$$

$$\mathbf{u}_{k+1} := \mathbf{u}_k + (\mathbf{h}_{k+1} - \mathbf{q}_{k+1}) \quad (21c)$$

Thus, the whole optimization procedure to find the minimum of \mathcal{L} involves iterative steps which alternate between minimization over \mathbf{q} and \mathbf{h} , while updating the scaled dual variable. By introducing two extra variables $\tilde{\mathbf{q}} = \mathbf{h} - \mathbf{u}$ and $\tilde{\mathbf{h}} = \mathbf{q} + \mathbf{u}$,

expressions for the ADMM iterations can be written in the following way:

$$\hat{\mathbf{q}}_{k+1} := \underset{\mathbf{q} \in \mathbb{C}^{(N \times 1)}}{\operatorname{argmin}} \left\{ \mathcal{D}(\mathbf{q}) + \frac{\rho}{2} \|\mathbf{q} - \mathbf{q}_k\|_2^2 \right\} \quad (22a)$$

$$\hat{\mathbf{h}}_{k+1} := \underset{\mathbf{h} \in \mathbb{C}^{(N \times 1)}}{\operatorname{argmin}} \left\{ \lambda \mathcal{R}(\mathbf{h}) + \frac{\rho}{2} \|\mathbf{h} - \mathbf{h}_k\|_2^2 \right\} \quad (22b)$$

$$\mathbf{u}_{k+1} := \mathbf{u}_k + (\mathbf{h}_{k+1} - \mathbf{q}_{k+1}) \quad (22c)$$

Here, sub-problem (22a) defines an inversion operator of the forward model and depends only on the forward model and measurements. Sub-problem (22b) is the denoising operator on $\tilde{\mathbf{h}}_k$ and depends on the selection of the regularization function \mathcal{R} (i.e., priors). (22c) is the auxiliary updates of ADMM. The alternating sub-minimization steps of ADMM are illustrated in a block diagram in Figure 2.

It is worthwhile to note that the model optimization is decoupled from the prior optimization in this framework. This flexible modularity of ADMM allows for plug-and-playing of different denoisers in a fully isolated manner, so that model/data optimization steps remain unaffected.

3.2. Solutions for ADMM Sub-Problems

An analytical solution exists for sub-problem (22a). We take the partial derivative of the objective function to find the minimum of (22a) with respect to \mathbf{q} and get the following gradient vector $\nabla \mathbf{q}$:

$$\nabla \mathbf{q} = -2\mathbf{T}^H \mathbf{r} + 2\mathbf{T}^H \mathbf{T} \mathbf{q} + \rho(\mathbf{I} \mathbf{q} - \tilde{\mathbf{q}}) \quad (23)$$

Arranging (23), we get

$$\nabla \mathbf{q} = (2\mathbf{T}^H \mathbf{T} + \rho \mathbf{I}) \mathbf{q} - (2\mathbf{T}^H \mathbf{r} + \rho \tilde{\mathbf{q}})$$

By equating $\nabla \mathbf{q}$ to zero, we get the first-order optimality condition as follows:

$$\underbrace{(2\mathbf{T}^H \mathbf{T} + \rho \mathbf{I})}_{\mathbf{A}} \mathbf{q} = \underbrace{(2\mathbf{T}^H \mathbf{r} + \rho \tilde{\mathbf{q}})}_{\mathbf{b}} \quad (24)$$

with a closed-form solution of:

$$\hat{\mathbf{q}} = (\mathbf{A})^{-1} \mathbf{b} = (2\mathbf{T}^H \mathbf{T} + \rho \mathbf{I})^{-1} (2\mathbf{T}^H \mathbf{r} + \rho \tilde{\mathbf{q}}) \quad (25)$$

The linear system of equations described by $\mathbf{A} \mathbf{q} = \mathbf{b}$ in (24) can be solved using any linear system solver, and we prefer to use the conjugate-gradient algorithm. The role of ρ here is to control the balance between data-fidelity error and priors of \mathbf{q} .

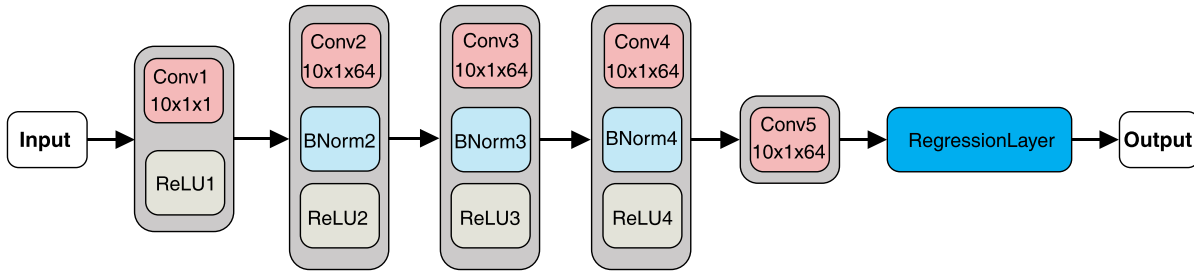


FIGURE 3. Convolutional neural network architecture.

Note that in case $\rho = 0$, the problem is simplified to the least-squares regression with the following pseudoinverse solution:

$$\hat{\mathbf{q}} = (\mathbf{T}^H \mathbf{T})^{-1} \mathbf{T}^H \mathbf{r} \quad (26)$$

Note that if $\mathcal{R}(\mathbf{h}_k)$ in sub-problem (22b) is chosen as $\mathcal{R}(\mathbf{h}_k) = -\log(p(\mathbf{h}_k))$, then (22b) is the MAP estimator designed to remove additive Gaussian noise with the power of $\sigma^2 = \lambda/\rho$ from the noisy version of \mathbf{h} and acts as Gaussian denoiser on $\tilde{\mathbf{h}}$, trying to minimize the residue between clean and noisy signal using priors $\tilde{\mathbf{h}}_k$.

Note that sub-problem (22b) only depends on the priors. Since the prior optimization step given by sub-problem (22b) is basically an denoising operator, it can be approximated by any denoiser. In [11], authors propose to use any off-the-shell

denoising algorithm for this problem in what they call the Plug-and-Play ADMM framework. Motivated by this, we use a similar approach where we utilize a convolutional neural network (CNN) as in [17] to tackle the sub-problem (22b). After successful training, this network takes one-dimensional noisy range profile data as input and generates a denoised version at the output. Essentially, the network is trained to learn the process of denoising radar range profiles. Through this training, the network learns the complex and intricate spatial patterns present in the data.

A simplified architecture of the implemented network is shown in Figure 3. The first layer has a convolution layer and a ReLU layer and is followed by three Convolution-Batch normalization-ReLU layers. At the output, a regression layer is used to perform the final mapping. Training of this network is discussed in detail in Section 4. In Figure 4, a flowchart illustrating the ADMM updates is presented. Here, a single iteration of the ADMM framework is depicted, and this process continues until convergence. The ADMM procedure initiates with conventional fast Fourier transform (FFT)-based estimation, succeeded by a model-data alignment update and priors update via a denoising CNN. The pre-trained CNN processes noisy range profiles and generates a cleaned version for utilization in the subsequent iteration of ADMM.

To implement the ADMM flow outlined in Figure 4, Algorithm 1 is implemented in MATLAB. The ADMM iterations terminate either when the change in the auxiliary variable \mathbf{u} becomes smaller than the specified tolerance value, i.e., $\|\mathbf{u}^{(k+1)} - \mathbf{u}^{(k)}\|_2^2 < \epsilon$, or when the maximum number of ADMM iterations is reached.

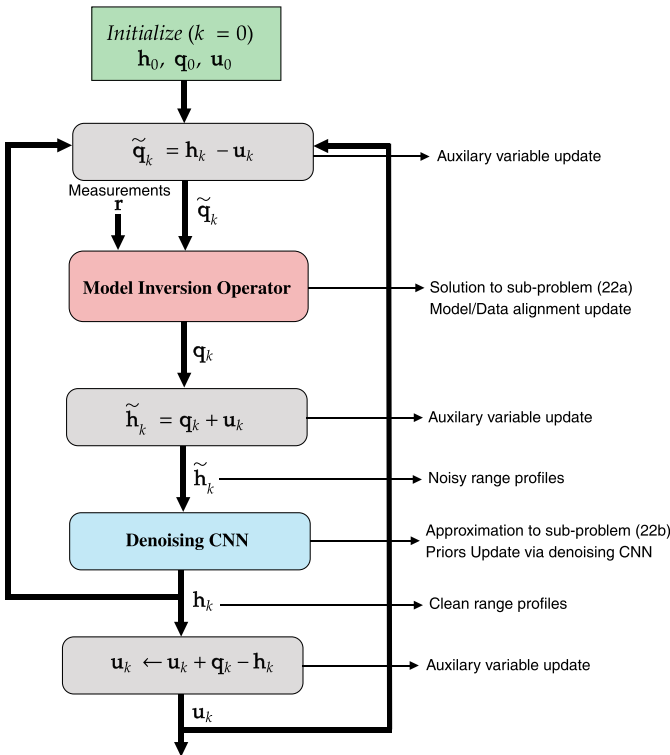


FIGURE 4. Flow chart describing the ADMM iterations for model/data and priors update. Model/data update is executed by computing the solution in (25), and priors update is accomplished through a denoising CNN.

Algorithm 1 PnP ADMM algorithm for radar range profile reconstruction

```

Require:  $\mathbf{T}, \mathbf{y}$ 
 $\mathbf{q} \leftarrow \mathbf{T}^{-1} \mathbf{r}$  - Initial estimation with FFT
 $\mathbf{h} \leftarrow \mathbf{q}, \mathbf{u} \leftarrow \mathbf{0}$ 
while stopping criteria is not satisfied do
     $\tilde{\mathbf{q}} \leftarrow \mathbf{h} - \mathbf{u}$ 
     $\mathbf{q} \leftarrow$  solution of (22a) - Model/data update
     $\tilde{\mathbf{h}} \leftarrow \mathbf{q} + \mathbf{u}$ 
     $\mathbf{h} \leftarrow$  solution of (22b) - Priors update
     $\mathbf{u} \leftarrow \mathbf{u} + \mathbf{q} - \mathbf{h}$  - Auxiliary update
end while
return  $\mathbf{h}$ 
    
```

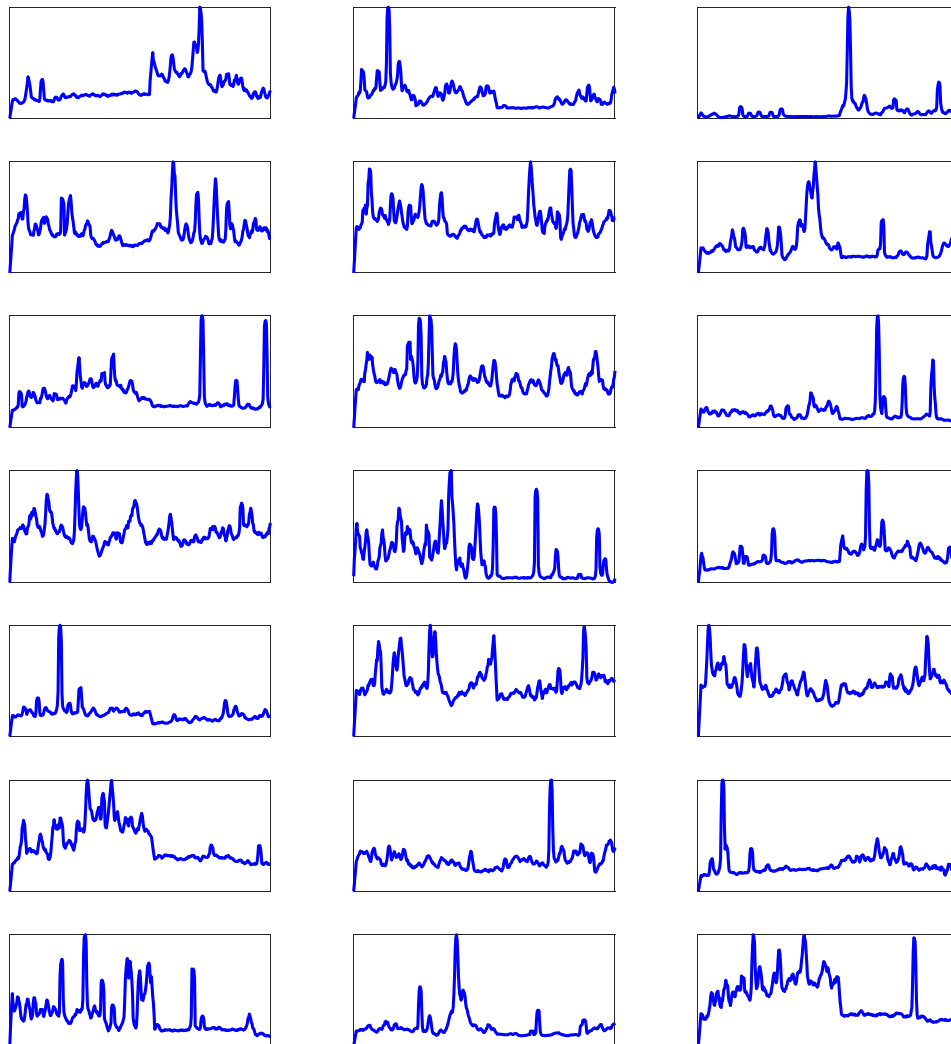


FIGURE 5. A sample set of range profiles used in the simulations. (Horizontal axis is the range axis and vertical axis is the radar reflectivity magnitude).

4. NUMERICAL RESULTS

In order to test the performance of the ADMM based range profile reconstruction framework described in the previous section, we use the Gotcha Volumetric SAR Data Set, Version 1.0 which is publicly available in [21]. The data set contains SAR phase history data from a scene consisting of numerous civilian vehicles and calibration targets. Measurements are taken using an X-band radar with a bandwidth of 640 MHz from a 360° azimuth coverage at 8 different elevation angles with all possible polarization combinations. The data set comprises phase history data collected during each 1° scan, comprising 117 pulses with complex IQ samples. Since the radar measurements are collected in the Fourier space, conversion from measurements to range profile data is carried out by Fourier Transform as suggested by relation (7). Measurement model \mathbf{T} for this setup is therefore an inverse Fourier Transform matrix.

Using the Gotcha SAR phase history data, we derive our own data set of range profiles in the following way: we first convert each and every fast-time radar data in the phase history matrix

to a range profile by taking its DFT. Since the DFT result will be complex-valued, we take the absolute value of each of these 117 range profiles. Then, we perform a non-coherent pulse integration using all the the range profiles formed in order to get a relatively less noisy range profile data and finally pass it through a low-pass filter to further reduce the background noise in the reconstructed range profiles. A sample set of range profiles obtained from the phase history data set is shown in Figure 5. The total number of range profile samples obtained in the described way is 11520. Note that the reconstructed range profile data is real-valued. This might mirror situations where the radar footprint is narrow and there are only dominant scatterers on the radar footprint.

The reason for us to make our own data set for range profile data is that we want to simulate our own measurements based on these generated range profiles considering different levels of measurement bandwidth and noise. We simulate our own measurements by using the measurement model given in (11) and use a DFT matrix as the measurement model \mathbf{T} , and \mathbf{w} is chosen to be complex white noise. In order to test the perfor-

Parameter	Value	Parameter	Value
Epoch	100	L2 Regularization	0.001
Initial Learning Rate	0.1	Learning Rate Drop Period	10
Momentum	0.9	Learning Rate Drop Factor	0.1

TABLE 1. Training parameters for CNN.

mance of the proposed framework under different noise and bandwidth conditions, we consider six different bandwidth levels (5%, 10%, 15%, 20%, 25%, 30%) and six different relative noise levels ($\sigma_0, 2\sigma_0, 3\sigma_0, 4\sigma_0, 5\sigma_0, 6\sigma_0$). Bandwidth level is adjusted by means of a mask chosen around the middle row of the DFT matrix, which corresponds to DC frequency. For example, 5% data availability case is obtained by slicing 20 rows around the center row (rows corresponding to the low frequencies) of the 400×400 DFT matrix. Hence for 5% data availability, we use a 20×400 DFT matrix as a forward measurement model. The reconstruction problem would be estimating radar range profile of 400 range cells from 20 radar measurement samples, which corresponds to solving a highly under-determined system of equations.

Data set for the implemented CNN consists of noisy and clean range profile data pairs. The noisy range profile data is obtained by adding measurement noise with a variance randomly drawn from these 6 noise power levels. For the training of CNN, we divide the range profile data set into a training set (80%), a test set (10%), and a validation set (10%). We use Stochastic Gradient Descent with Momentum (SGDM) as an optimizer for the training of the network. Other training parameters are summarized in Table 1. Training is performed in MATLAB 2020 using the Deep Learning Toolbox running on a NVIDIA GeForce MX250 GPU. The loss of the network during 100 epochs of training is plotted in Figure 6. To gauge the effectiveness of our ADMM-based range profile reconstruction, we utilize the Mean Squared Error (MSE) metric. This metric calculates the average of the squared differences between a test vector and the reference vector as follows:

$$\text{MSE} = \frac{1}{N} \|\hat{\mathbf{q}} - \mathbf{q}^{\text{ref}}\|_2^2 = \frac{1}{N} \sum_{i=1}^N (\hat{q}_m(i) - q_m^{\text{ref}}(i))^2$$

We evaluate the performances of different methods on the test data set considering different measurement bandwidths and noise variances. We compare the proposed range profile formation method (ADMM-CNN) with a conventional FFT and l_2 -norm regularized reconstruction, as well as ADMM based reconstruction with two different denoisers, namely Total-variation (TV) [14] and Recursive-filter (RF) [15]. We

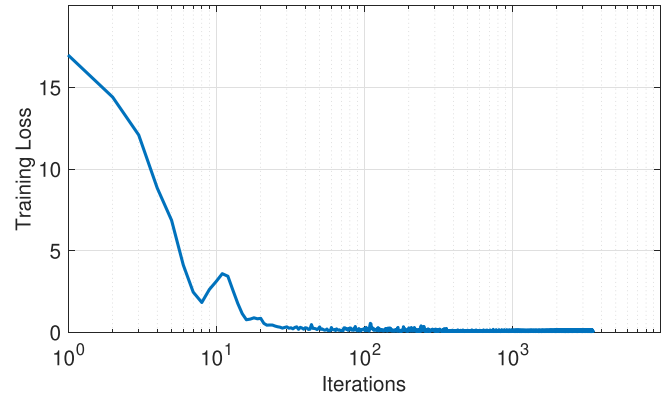


FIGURE 6. Loss during training of the network.

call these methods ADMM-TV, ADMM-RF depending on the denoiser used. Among these methods, FFT-based reconstruction is the conventional and most commonly employed approach, relying solely on the Fourier measurement matrix without the use of any regularization techniques. l_2 -norm regularized reconstruction on the other hand regularizes the solution in l_2 -norm sense. The other methods are implemented within the ADMM framework, differing only in the denoising technique employed to address the prior optimization step in (22b).

In Figure 7, we present a representative range profile reconstructed through various methods, with corresponding Mean Squared Error (MSE) values displayed atop each subplot. Figure 7(a) shows an illustrative range profile reconstructed from simulated measurements at three distinct noise levels and the full bandwidth. In contrast, Figure 7(b) depicts a reconstruction experiment with three different bandwidth levels without any measurement noise. In these figures, columns represent distinct reconstruction methods, each denoted at the top, while rows signify various measurement conditions, including the presence of measurement noise and bandwidth variations. The original range profile is represented in red, while the range profiles reconstructed from simulated measurements are depicted in blue.

Upon close examination of these plots, it becomes evident that conventional FFT-based reconstruction and l_2 -norm regularized reconstruction suffer significantly under conditions of low bandwidth and/or high measurement noise. In contrast, the ADMM-based reconstruction methods consistently deliver superior performance. Notably, among the ADMM-based approaches, employing a CNN as a denoiser in the prior optimization step of the ADMM framework yields the most outstanding reconstruction results. ADMM-CNN method stands out for its ability to effectively capture the distinct peaks within the range profile data while substantially mitigating noise in the signal, resulting in the lowest MSE across all test cases. It is noteworthy that the ADMM-CNN algorithm exhibits remarkable resilience, showcasing promising reconstruction performance even in scenarios featuring limited measurement data or high levels of measurement noise.

For a comprehensive evaluation of the ADMM-CNN range profile reconstruction method and to establish a statistical

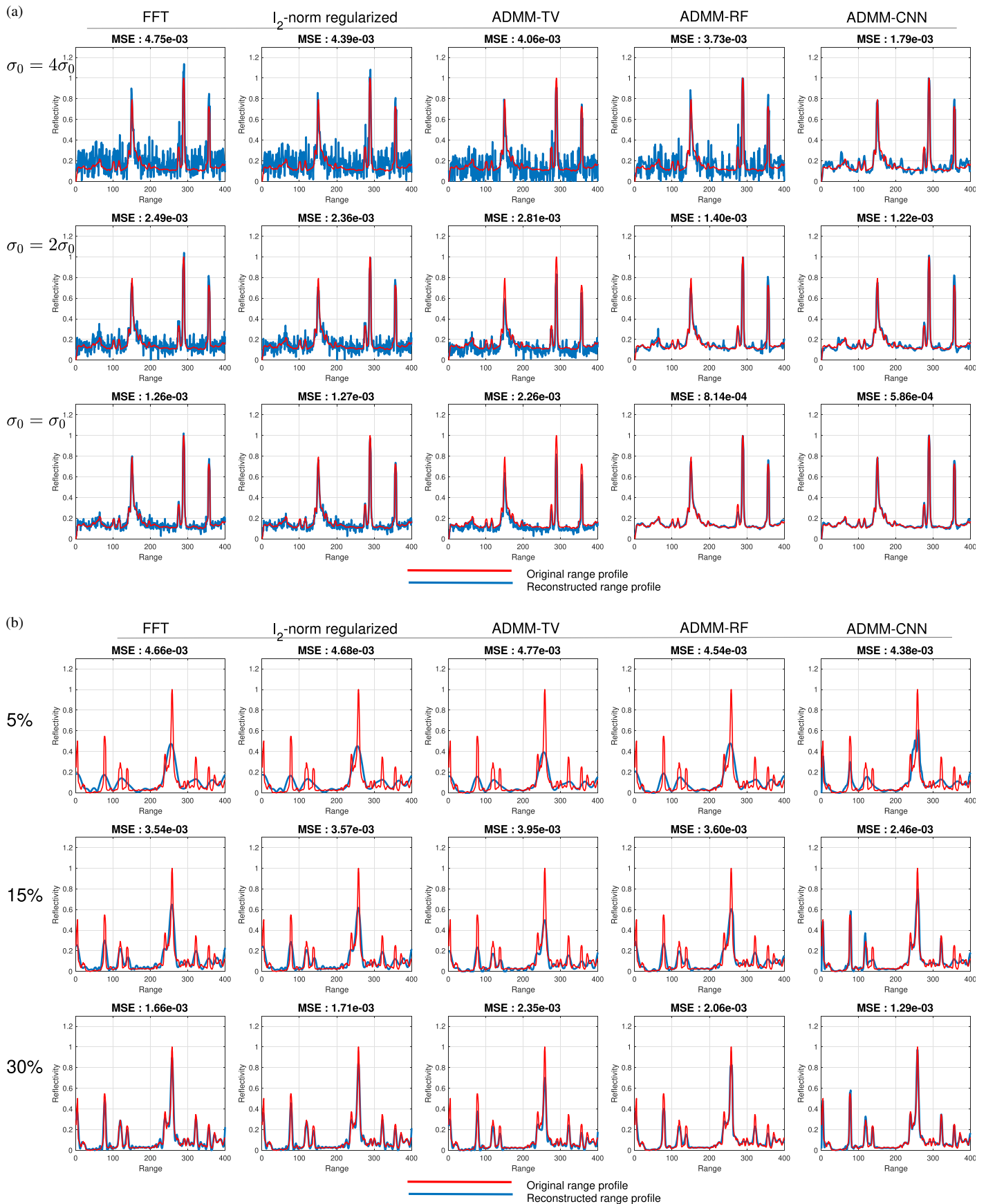


FIGURE 7. Comparison of various range profile reconstruction approaches on an example range profile in terms of MSE performance under different noise and bandwidth conditions. (a) Reconstruction at three different measurement noise values (full-bandwidth). (b) Reconstruction at three measurement bandwidth values (no measurement noise present).

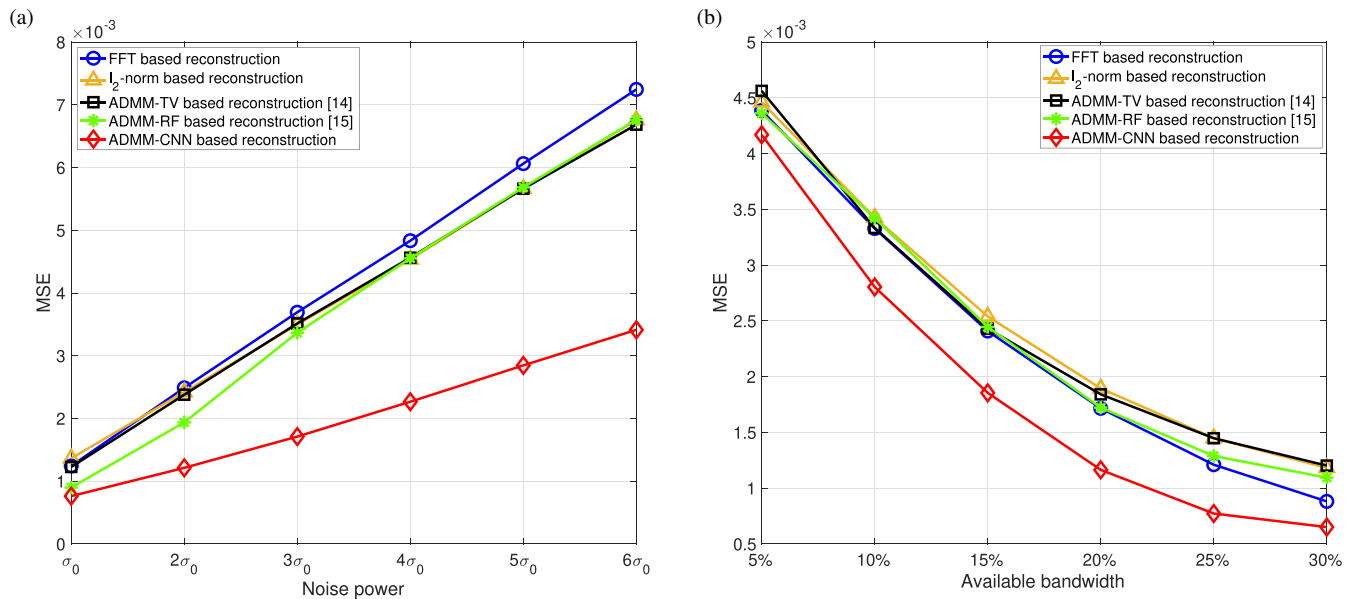


FIGURE 8. MSE performance comparison of different reconstruction methods under different bandwidth availability and measurement noise conditions. (a) MSE as a function of noise power. (b) MSE as a function of measurement bandwidth.

overview of its MSE performance, we apply each reconstruction method over a small subset of the test dataset, comprising 100 range profile samples. We then compute the MSE values for each sample, calculate their average. We present the results in Figure 8, which encapsulate the MSE performance across all 100 range profiles. Figure 8(a) shows the average MSE of each method with respect to noise power, whereas Figure 8(b) shows the average MSE with respect to measurement bandwidth. The average MSE values further affirm that the ADMM-CNN method excels in terms of reconstruction performance when compared to the other investigated reconstruction methods under the examined measurement conditions.

5. CONCLUSIONS

In this study, we explore the radar range profile reconstruction problem using a Plug-and-Play ADMM framework. We derive the observation model tailored for side-looking FMCW radar. We formulate ADMM steps, where a denoising CNN acts as a solver for the prior optimization subproblem. We showcase the potential of utilizing a denoising CNN as a powerful tool to learn the intricate spatial patterns embedded within the range profile data and use it as a means of regularization. Through comprehensive simulations, we substantiate the effectiveness of employing deep learning networks as a regularization mechanism within the ADMM framework for radar range profile formation, as we present extensive performance evaluation of ADMM framework with CNN regularizer in comparison to alternative methods across diverse measurement scenarios. We also demonstrate the potential of using a CNN trained on a dataset with mixed SNR levels while ensuring robust performance across varying SNR conditions. Remarkably, among the reconstruction techniques under investigation, the ADMM approach with CNN emerges as the most successful solution

for radar range profile reconstruction problem in terms of MSE performance.

REFERENCES

- [1] Akçapınar, K. and S. Baykut, "CM-CFAR parameter learning based square-law detector for foreign object debris radar," in *2018 48th European Microwave Conference (EuMC)*, 1441–1444, 2018.
- [2] Jacobs, S. P. and J. A. O'Sullivan, "Automatic target recognition using sequences of high resolution radar range-profiles," *IEEE Transactions on Aerospace and Electronic Systems*, Vol. 36, No. 2, 364–381, 2000.
- [3] Ganis, A., E. M. Navarro, B. Schoenlinner, U. Prechtel, A. Meusling, C. Heller, T. Spreng, J. Mietzner, C. Krimmer, B. Haerberle, *et al.*, "A portable 3-D imaging FMCW MIMO radar demonstrator with a 24×24 antenna array for medium-range applications," *IEEE Transactions on Geoscience and Remote Sensing*, Vol. 56, No. 1, 298–312, 2018.
- [4] Leuschen, C. J. and R. G. Plumb, "A matched-filter-based reverse-time migration algorithm for ground-penetrating radar data," *IEEE Transactions on Geoscience and Remote Sensing*, Vol. 39, No. 5, 929–936, 2001.
- [5] Zhao, S. and I. L. Al-Qadi, "Development of regularization methods on simulated ground-penetrating radar signals to predict thin asphalt overlay thickness," *Signal Processing*, Vol. 132, 261–271, 2017.
- [6] Cetin, M. and W. C. Karl, "Feature-enhanced synthetic aperture radar image formation based on nonquadratic regularization," *IEEE Transactions on Image Processing*, Vol. 10, No. 4, 623–631, 2001.
- [7] Miran, E. A., F. S. Oktem, and S. Koc, "Sparse reconstruction for near-field MIMO radar imaging using fast multipole method," *IEEE Access*, Vol. 9, 151 578–151 589, 2021.
- [8] Boyd, S., N. Parikh, E. Chu, B. Peleato, and J. Eckstein, "Distributed optimization and statistical learning via the alternating direction method of multipliers," *Foundations and Trends® in*

- Machine Learning*, Vol. 3, No. 1, 1–122, 2011.
- [9] He, J., Y. Yang, Y. Wang, D. Zeng, Z. Bian, H. Zhang, J. Sun, Z. Xu, and J. Ma, “Optimizing a parameterized plug-and-play ADMM for iterative low-dose CT reconstruction,” *IEEE Transactions on Medical Imaging*, Vol. 38, No. 2, 371–382, 2019.
- [10] Güven, H. E., A. Güngör, and M. Çetin, “An augmented Lagrangian method for complex-valued compressed SAR imaging,” *IEEE Transactions on Computational Imaging*, Vol. 2, No. 3, 235–250, 2016.
- [11] Sreehari, S., S. V. Venkatakrishnan, B. Wohlberg, G. T. Buzzard, L. F. Drummy, J. P. Simmons, and C. A. Bouman, “Plug-and-play priors for bright field electron tomography and sparse interpolation,” *IEEE Transactions on Computational Imaging*, Vol. 2, No. 4, 408–423, 2016.
- [12] Chan, S. H., X. Wang, and O. A. Elgandy, “Plug-and-play ADMM for image restoration: Fixed-point convergence and applications,” *IEEE Transactions on Computational Imaging*, Vol. 3, No. 1, 84–98, 2017.
- [13] Dabov, K., A. Foi, V. Katkovnik, and K. Egiazarian, “Image denoising by sparse 3-D transform-domain collaborative filtering,” *IEEE Transactions on Image Processing*, Vol. 16, No. 8, 2080–2095, 2007.
- [14] Chan, S. H., R. Khoshabeh, K. B. Gibson, P. E. Gill, and T. Q. Nguyen, “An augmented Lagrangian method for total variation video restoration,” *IEEE Transactions on Image Processing*, Vol. 20, No. 11, 3097–3111, 2011.
- [15] Gastal, E. S. L. and M. M. Oliveira, “Domain transform for edge-aware image and video processing,” *ACM Trans. Graph.*, Vol. 30, No. 4, 1–12, Jul. 2011.
- [16] Buades, A., B. Coll, and J.-M. Morel, “A non-local algorithm for image denoising,” in *2005 IEEE Computer Society Conference on Computer Vision and Pattern Recognition (CVPR’05)*, Vol. 2, 60–65, 2005.
- [17] Alver, M. B., A. Saleem, and M. Çetin, “Plug-and-play synthetic aperture radar image formation using deep priors,” *IEEE Transactions on Computational Imaging*, Vol. 7, 43–57, 2020.
- [18] Li, X., X. Bai, Y. Zhang, and F. Zhou, “High-resolution ISAR imaging based on plug-and-play 2D ADMM-net,” *Remote Sensing*, Vol. 14, No. 4, 901, 2022.
- [19] Gao, X., C. Xiao, and C. Zhang, “Plug-and-play ADMM for sparse ISAR imaging,” in *2021 CIE International Conference on Radar (Radar)*, 6–10, 2021.
- [20] Cetin, M., “Feature-enhanced synthetic aperture radar imaging,” Ph.D. dissertation, Boston University, 2001.
- [21] Gotcha volumetric SAR data set, Version 1.0.